3-D crustal VS model of western France and the surrounding regions using Monte-Carlo inversion of seismic noise cross-correlation dispersion diagrams

I Gaudot, Éric Beucler, A. Mocquet, M Drilleau, M Haugmard, Mickaël Bonnin, Geoffrey Aertgeerts, D Leparoux

To cite this version:

I Gaudot, Éric Beucler, A. Mocquet, M Drilleau, M Haugmard, et al.. 3-D crustal VS model of western France and the surrounding regions using Monte-Carlo inversion of seismic noise cross-correlation dispersion diagrams. Geophysical Journal International, 2021, 224 (3), pp.2173-2188. 10.1093/gji/ggaa552 . hal-03161132

HAL Id: hal-03161132
https://hal.science/hal-03161132v1

Submitted on 21 Jan 2022

submitted to *Geophys. J. Int.*

3-D crustal V_S model of western France and the surrounding regions using Monte-Carlo inversion of seismic noise cross-correlation dispersion diagrams

I. Gaudot[1,2], É. Beucler[1], A. Mocquet[1], M. Drilleau[3], M. Haugmard[1], M. Bonnin[1],

G. Aertgeerts[4], D. Leparoux[5]

1 *Laboratoire de planétologie et géodynamique,*

UMR-CNRS 6112, Nantes University, University of Angers, France

2 *Now at BRGM, F-45060 Orléans, France*

3 *Institut Supérieur de l'Aéronautique et de l'Espace—SUPAERO, Toulouse, France*

4 *BRGM, F-97300 Cayenne, Guyane française*

5 *GERS-GeoEND, Univ Gustave Eiffel, Campus Nantes, IFSTTAR, F-44344 Bouguenais, France*

15 November 2020

Summary

Due to a too sparse permanent seismic coverage during the last decades, the crustal structure of western France and the surrounding regions is poorly known. In this study, we present a 3-D seismic tomographic model of this area obtained from the analysis of 2-year continuous data recorded from 55 broad-band seismometers. An unconventional approach is used to convert Rayleigh wave dispersion diagrams obtained from ambient noise cross-correlations into posterior distributions of 1-D V_S models integrated along each station pair. It allows to avoid the group velocity map construction step (which means dispersion curve extraction) while providing meaningful V_S posterior uncertainties. V_S models are described by a self-adapting and parsimonious parameterization using cubic Bézier splines. 1268 separately inverted 1-D V_S profiles are combined together using a regionalization scheme, to build the 3-D V_S model with a lateral resolution of 75 km over western France. The shallower part of the model (horizontal cross-section at 4 km depth) correlates well with the known main geological features. The crystalline Variscan basement is clearly associated with positive V_S perturbations while negative heterogeneities match the Mesocenozoic sedimentary basins. At greater depths, the Bay of Biscay exhibits positive V_S perturbations, which eastern and southern boundaries can be interpreted as the ocean-continent transition. The overall crustal structure below the Armorican Massif appears to be heterogenous at the subregional scale, and tends to support that both the South-Armorican Shear Zone and the Paris Basin Magnetic Anomaly are major crustal discontinuities that separate distinct domains.

Keywords: Europe, Tomography, Crustal imaging, Surface waves and free oscillations, Seismic interferometry, Inverse Theory

1 INTRODUCTION

The geology of France results from the succession of the Variscan orogeny (Paleozoic) and the Alpine orogeny (mid-Mesozoic to mid-Cenozoic), punctuated by an intense episode of extensional tectonics during the Mesozoic and Cenozoic. According to most geodynamical models, the Variscan orogeny in western Europe would result from the collision of two main continents: Gondwana to the South and Laurentia-Baltica to the North, sandwiching some microplates (Armorica, Avalonia) separated by oceanic suture [Matte, 2001; Ballèvre et al., 2009]. The French Variscan Massifs are the Armorican Massif, the Massif Central, the Vosges and the Ardennes, where the pre-Mesozoic basement crops out (Figure 1a). The Mesocenozoic episode of extension initiated the formation of the Paris basin, the Aquitaine basin and the Southeastern basin, which are the three main sedimentary basins in metropolitan

France. From 150 to 50 Ma, the counterclockwise rotation of the Iberian peninsula led to the formation of the Bay of Biscay. The Bay of Biscay is a “V-shape” oceanic basin located in southwestern France. The major geological feature of the western France is the Armorican Massif, which is a fragment of the Variscan orogeny isolated from the recent Alpine deformation. The Armorican Massif is divided by two NW-SE oriented Carboniferous shear zones (the North-Armorican Shear Zone and the South-Armorican Shear Zone, hereafter referred to as SASZ and NASZ, respectively, see Figure 1a)) into three main domains: (i) the North-Armorican domain, which is a preserved fragment of the Cadomian orogeny [D’Lemos et al., 1990], (ii) the Central- and (iii) the South-Armorican domains which have been affected by the Variscan orogeny. According to Ballèvre et al. [2009], the SASZ would be a major discontinuity which separates Armorica related terranes (including the Central- and North-Armorican domains) from Gondwana related terranes (including the South-Armorican domain).

The geology of the Armorican Massif and the surrounding regions have been extensively studied during the last century [Chantraine et al., 2003]. The development of geophysical experiments in the early 1970’s provided images of the structures at depth which greatly contributed to a better understanding of the geodynamic history of the area. Large Variscan thrusts cutting the entire pre-Mesozoic basement have been evidenced beneath the Celtic Sea and the British Channel [ECORS-BIRP experiment, Bois et al., 1991; Cloetingh et al., 2013], beneath the Paris basin near the Bray fault [ECORS experiment, Cazes et al., 1985, 1986], and in the South-Armorican domain near the SASZ [GéoFrance3-D-Armor project, Bitri et al., 2003, 2010; Martelet et al., 2004]. Moreover, steeply dipping thrust faults localized in the upper crust and related to the Cadomian orogeny were detected in the North-Armorican domain [GéoFrance3-D-Armor project, Bitri et al., 2001]. Active source seismic sounding results tend to support the presence of a relatively flat Moho (average depth of 30 +/- 5 km) beneath the Armorican Massif [Sapin & Prodehl, 1973; Matte & Hirn, 1988; Bitri et al., 2001, 2003, 2010] and the Paris basin [Cazes et al., 1985, 1986]. Moreover, it is generally admitted that the Moho is very shallow (< 20 km) in the Parentis oceanic basin, located in the heart of the Bay of Biscay [Pinet & Montadert, 1987]. The magnetic and gravity maps support the hypothesis that the Central- and North-Armorican domains belong to the same terrane bounded on the South by the SASZ, and on the East by the Bray fault located in the Paris basin [Autran et al., 1994]. Besides, the geophysical data suggest that the South-Armorican domain, the Massif Central and the Vosges are closely related [e.g. Baptiste et al., 2016]. Using L_g waves, Campillo & Plantet [1991] detected a NW-SE elongated region of attenuating material in the Central-Armorican domain, which is correlated with a zone of strong seismic heterogeneity in the crust [Matte & Hirn, 1988]. Arroucau et al. [2006] observed that old Variscan regions display a lower attenuation than young Alpine regions. More recently, the low frequency ($\simeq$ 1 Hz) absorption tomography results of Mayor et al. [2017] showed that the Mesocenozoic basins are associated with high absorption regions, whereas the Variscan regions are characterized with low absorption values.

During the last 20 years, the development of national permanent seismic networks as well as temporary seismic experiments shed light on the crustal structure beneath western Europe [e.g. Yang et al., 2007; Verbeke et al., 2012; Lu et al., 2018]. Those studies focused on central Europe (and for a lot of them, the Alps) where seismic stations coverage is the best. In 2011-2013, temporary networks of broad-band seismometers have been deployed in southwestern France, along the French Atlantic coast, and in northern Spain as part of the PYROPE [Chevrot & Sylvander, 2017] and IBERARRAY [Diaz et al., 2009] experiments. Using this dataset, Chevrot et al. [2014] performed a three-dimensional V_P tomography of the upper mantle structures beneath the Pyrenees and the surrounding regions. The tomography shows negative anomaly beneath the Massif Central and the segmentation of the lithosphere in southwestern France by major faults inherited from the Variscan orogeny. The V_S crustal structure of the Pyrenees and the surrounding regions was obtained from ambient noise surface wave tomography [Macquet et al., 2014]. The model exhibits clear seismic signatures correlated with known geological features. Six additional broad-band seismic stations have been deployed in the western France (Armorican Massif and western part of Parisian Basin) in order to extend the PYROPE network. They strongly contribute to a better resolution of the crustal structures in the targeted region (see black dashed-line rectangle in Figure 1a).

The synchronous deployments of temporary networks in addition to the permanent stations available at this time enable to use crustal imaging techniques based on empirical Green's function computation from seismic ambient noise cross-correlations [Campillo, 2006]. Surface waves are mainly reconstructed in the cross-correlations in the $1-50$ s period range, which makes the seismic ambient noise cross-correlation method a powerful tool for crustal imaging [Shapiro et al., 2005]. Most surface wave ambient noise tomography techniques rely on tracking the maximum of the envelope of the surface wave train filtered around a discrete period in order to find the group velocity dispersion curve [Levshin et al., 1989]. Nevertheless, the presence of several maxima at each period due to incoherent noise, multipathing and/or waves interference often poses severe problems to obtain smooth group velocity dispersion curves. Thus, (semi-) manual picking is recommended to prevent misleading results [Herrmann, 2013]. However, dense seismic networks lead to a huge amount of data which severely limits the possibility of a systematic visual inspection. Therefore, fully automatic methods have emerged, such as the FTAN (Frequency Time ANalysis) technique [Levshin & Ritzwoller, 2001; Bensen et al., 2007] which has been successfully used in many ambient noise tomographic studies. However, the main disadvantage of such approaches is that ad hoc user's criteria control the degree of smoothness of the dispersion curve. Depending on the user's choices, the resulting dispersion curve may display either unrealistic jumps or an oversmoothed shape. Moreover, the condition of smoothness is satisfied only in a restricted period band, resulting in truncated dispersion curves which potentially omit relevant information contained in the full period band. A further difficulty is the evaluation of dispersion curve uncertainties. The use of the stability of spatially clustered and temporally repeated measurements or the use of the signal to noise ratio as a proxy have been proposed to quantify uncertainties [Bensen et al., 2007; Nicolson et al., 2014]. Most of techniques assume a Gaussian distribution for the data uncertainties, but this approximation fails in many cases.

For instance, multipathing effects may result in a multimodal distribution. Therefore, it remains a challenge to get the group velocities uncertainties in a robust way.

The contributions of this study are twofold. First, we present a new surface wave inversion approach, which does not require group velocity dispersion picking and does not assume Gaussian uncertainties. Following the idea of Cauchie & Saccorotti [2012] and Panning et al. [2015], the proposed strategy relies on a Markov chain Monte-Carlo (McMC) inversion of the noise cross-correlation dispersion diagram for retrieving 1-D V_S variations with depth. Second, we present the first regional 3-D isotropic V_S model beneath western France and the surrounding area by combining data from temporary experiments and permanent national seismic stations. This article is organized as follows. In section 2, we present the data processing, with a special emphasis on the regional noise conditions and the pre-processing dedicated to the empirical Green's function retrieval. We hereafter present the non-linear McMC inversion procedure to get the 1-D path average V_S profiles from the noise cross-correlation dispersion diagrams. In section 4, we go into some details on the regionalization method used to build the 3-D V_S model. Finally, the major features of the V_S model are discussed and compared to previous geophysical results.

2 DATA PROCESSING

The seismic data come from a subset of 55 broad-band seismological stations belonging to the previously described temporary networks and three permanent national networks (RESIF[⋆], British Geological Survey, and Irish National Seismic Network). Figure 1b shows the station locations and technical details are summarized in the Supplementary Material 1. We used data between September, 2011 and December, 2013 recorded on the vertical component and filtered between the 2.5-50 s period band. The analysis of the horizontal components is beyond the scope of the paper which focuses on tomography based on vertical compo-

---

[⋆] French permanent network including RLBP, Geoscope and CEA-LDG stations nent Rayleigh waves. The total of 55 stations corresponds to 1485 interstation pairs, with a minimum and maximum path length of 25 km and 1631 km, respectively.

The empirical Green's function builds up after a sufficient self-averaging process which is provided by a random/uniform spatial distribution of the noise sources as well as scattering due to crustal heterogeneities [Campillo, 2006]. This is achieved by cross-correlating long time series, since the spatial distribution of the oceanic noise sources varies with time. In practice, an averaging over cross-correlations of single short duration time windows is usually realized. However, high energetic signals due to short transient events (such as earthquakes or oceanic storms) and signals due to persistent localized source [e.g. Gaudot et al., 2016] can contaminate the cross-correlation results. Therefore, dedicated processing schemes based on a good knowledge of the regional ambient noise properties must be used to ensure the emergence of unbiased empirical Green's functions.

2.1 Empirical Green's function emergence in an ocean-edge context

The seismic network (Figure 1b) is surrounded by the North Atlantic ocean, the North sea, the Baltic sea, and the Mediterranean sea, where active sources of seismic noise occur in the 1-30 s period band over the whole year [Friedrich et al., 1998]. Furthermore, a significant amount of seismic noise coming from eastern Europe has been observed at periods > 20 s [Yang & Ritzwoller, 2008]. The oceanic seismic noise sources in western Europe exhibit a high variability in space, time and frequency [Chevrot et al., 2007; Beucler et al., 2015], and thus strong ambient noise emerges from many directions when considering long durations, even though a dominant energy coming from the North Atlantic ocean is clearly observed at periods < 10 s [Ermert et al., 2015]. At periods > 10 s, the seismic noise energy tends to be more isotropic and displays less seasonal variations [Yang & Ritzwoller, 2008]. Therefore, the noise conditions of the study region are rather favorable for the reconstruction of the empirical Green's function in the 2.5-50 s period band. The low level of seismicity of the study area implies that transient energetic seismic arrivals due to regional and global earthquakes dominate the spurious signal to remove. In such case, procedures which consist in disregarding completely [1-BIT normalization, Campillo & Paul, 2003] or partially [running absolute mean, referred to as RAM, Bensen et al., 2007] the amplitude information of the time series prior to the cross-correlation, are well suited. In the frequency domain, spectral whitening is usually applied to reduce the influence of monochromatic signals [Bensen et al., 2007].

Considering the previous statements, the data processing is organized as follows. First, the continuous records at each station is segmented into non-overlapping 24 hr long windows. The windows with less than 90% of data are rejected, and the possible remaining gaps are linearly interpolated. The data at each station are then decimated to a uniform sampling rate of 1 Hz using an appropriate anti-aliasing filter. After removing the daily mean and trend, the instrument response is removed in the 2.5-50 s period band. Then, the temporal amplitudes are smoothed using a RAM normalization with a normalization window width of 25 s. We tested several RAM normalization window widths (5 s, 11 s, 17 s, 25 s), and the 1-BIT method (i.e normalization window width equals 1 s). We found that a width of 25 s (half of the maximum period considered) gives the best results in terms of signal-to-noise ratio, and that the 1-BIT normalization is significantly less performant than the RAM normalization. Spectral whitening is then applied, which means that the amplitude spectrum is divided by itself in the 2.5-50 s period band to reach a value of 1, and the other spectral amplitudes are set to 0. All the synchronous pre-processed 24 hr long windows are then cross-correlated. The daily cross-correlations are stored in the time domain from -3600 s to 3600 s. Finally, the available single cross-correlations are linearly stacked in the time domain to produce a unique long-term average cross-correlation for each station pair. The Figure 2 shows that most of the cross-correlations displays a clear emergent signal in a time window defined by arrival times corresponding to typical surface-wave group velocities (gray lines). As expected, the amplitude symmetry of the emergent signal in the cross-correlation strongly depends on the station pair orientation. For NW-oriented pairs, the amplitude of the emergent signal is higher in positive time lags than in negative time lags. For NE-oriented pairs, emergent signals with similar amplitude are observed at both negative and positive time lags. Moreover, short periods dominate the emergent signal for NW-oriented pair compared to NE oriented pairs. The empirical Green's function emergence is evaluated using the signal-to-noise ratio, hereafter referred to as SNR. It is defined as the ratio of the maximum amplitude of the Rayleigh wave to the rms amplitude of the noise in a 1000 s time window length, starting 200 s after the Rayleigh wave train. We show in Figure 3 that the SNR strongly depends on the azimuth. The azimuthal distribution of the SNR is related to the distribution of the incoming seismic noise energy [Stehly et al., 2006]. The polar distribution of SNR shown in Figure 3 indicates of dominant arrival of seismic noise energy coming from the North-West of the array, which is perfectly consistent with the North Atlantic ocean influence. However, one may also notice that whatever the angle the minimum SNR value is 8. This indicates that although there is a strong noise directivity pattern the requirements to reliably reconstruct empirical Green's functions are fulfilled, mostly thanks to the long duration time-series.

2.2 Selection criteria for empirical Green's functions

The cross-correlations with a SNR < 5 in the causal and anticausal part are rejected to guarantee than the dispersion diagram computation is performed on emergent Rayleigh wave trains. The selected cross-correlations are symmetrized (that is by stacking their causal and time-reversed anticausal signals to get a unique signal with a enhanced SNR, see Figure 4a). The cross-correlations are bandpass filtered between 5 s period and T_{max}, where T_{max} vary for each station-pair ensuring that - for a group velocity range of 2–5 km/s - at least three wavelengths can exist within the corresponding interstation distance [Bensen et al., 2007]. The paths associated with $T_{max} < 15$ s are discarded to avoid the analysis of too narrow frequency bandwidth empirical Green's functions. A total of 1268 empirical Green's functions out of the 1485 initial cross-correlations dataset are retained after the SNR and wavelength selection criteria.

3 NON-LINEAR EXPLORATION OF RAYLEIGH GROUP VELOCITY DISPERSION DIAGRAMS

3.1 Data space

As shown in Figure 4a, the empirical Green's function obtained by the ambient noise cross-correlation between vertical component records is dominated by a Rayleigh surface wave dispersive signal. For several reasons such as narrow band filtering side effects and/or multipathing, the step which consists in determining the most likely group velocity curve for a given path, by multiple filtered envelopes, can be strongly biased. For studies which are using empirical Green's function as real input waveform, the seismic ambient noise properties may also affect the reconstruction quality which can prevent to reliably pick a continuous group velocity curve over the whole frequency range [e.g. Macquet et al., 2014]. On the other hand, for studies which are using deterministic sources such as earthquakes, the source frequency can affect if one wants to select the continuous ridge (of a given branch). Some recent improvements can help to avoid this pitfall [Kolínský et al., 2019] but the velocity curve variances do not always reflect the complexity of a real data dispersion diagram. In order i) to handle the signal complexity in the time-frequency domain and ii) to provide reliable uncertainties, we introduce a new approach to explore a dispersion diagram without picking any group velocity curve. As many other studies, the input waveform is converted into a dispersion plot by using multiple narrow band-pass filters and the station pair distance. The novelty of our approach is to consider the whole dispersion diagram as the data space. The envelope of each resulting filtered waveform is seen as a probability density function (pdf) of possible group velocity values and the data space is then a collection of individual pdf (Figure 4b).

3.2 Non-linear inversion scheme

3.2.1 Inverse procedure framework

The inverse procedure we present in this section has some differences compared to the classical way of inferring 3-D models. Most of tomographic studies using surface waves (fundamental and/or higher modes) need a stage which is the construction of group/phase velocity maps [Barmin et al., 2001; Sabra et al., 2005; Ekström, 2011, among many others] to further convert local group/velocities perturbations into 1-D models [e.g. Ritzwoller & Levshin, 1998; Shapiro et al., 2005; Nishida et al., 2009; Kolínský et al., 2014]. This step can be made since an ensemble of individual velocity curves are extracted from the initial waveforms. In our case, we consider that if a given waveform (obtained from ambient noise cross-correlation or from a real earthquake seismogram) is a resultant of the wave field travelling along a given ray path then it might be possible to directly infer the probability of all 1D models that fit the data. In a way, this approach has some common points with the partition waveform [Nolet, 1990; Lebedev et al., 2005]. It means that a given trial 1-D V_S model can be uniquely turned into a group velocity curve and the fit of this curve in the data space (i.e. the whole dispersion diagram) enables to measure the pertinence (i.e. the likelihood) of the model. This can be achieved since each group velocity curve intersect the ensemble of group velocity pdf for all frequencies of the dispersion diagram (Figure 4b).

Following Tarantola [2005], the solution of an inverse problem can be described as the *a posteriori* pdf $\sigma(\mathbf{m})$ in the model space M, such as

$$\sigma(\mathbf{m}) \propto \rho_M(\mathbf{m})\ L(\mathbf{m}), \tag{1}$$

where $\rho_M(\mathbf{m})$ is a pdf defined in the model space that carries our *a priori* information on models $\mathbf{m}$, and $L(\mathbf{m})$ is the likelihood function, which gives a measure of how good a model $\mathbf{m}$ is in explaining the observed data. Assuming the observations to be independent and that modelling uncertainties may be neglected, the likelihood is defined as

$$L(\mathbf{m}) = \prod_{\mathrm{i}=1}^{nw} \rho_D^{\mathrm{i}} = \sum_{i=1}^{nw} \log(\rho_D^{\mathrm{i}}), \tag{2}$$

where ρ_D^{i} is the intersection value of the theoritical group velocity dispersion curve computed for a given trial 1-D V_S model, and the corresponding individual pdf computed for the period index i in the data space D, where $i = 1, \dots, nw$, with nw is the total number of narrow band-pass filters. The sum over log values is used to prevent numerical instabilities. Since we consider that individual pdf in the data space may have arbitrary shape, the likelihood formulation in Equation 2 differs from classical methods which rely on a L-norm misfit computation.

3.2.2 Model parameterization and prior on parameters

In this study, we infer 1-D V_S probabilities for quite long paths (> 180 km). Given the depth variability of the strong velocity contrasts expected over the studied area [see Chevrot et al., 2014, for the topography of the Moho], velocity gradients rather than discontinuities are likely to be detected in the path average velocity profiles. Therefore, we think that a model parameterization that allows both continuous velocity variations with depth and discontinuities can be well-suited. Following Drilleau et al. [2013], we choose a succession of cubic Bézier curves to describe the overall velocity profile (Figure 5). Each Bézier curve is based on a set of four control points, noted P_{j0}, P_{j1}, P_{j2}, P_{j3}, where $j = 0, \dots, N$ denotes the index of the curve. Each Bézier curve does not pass generally through P_{j1} and P_{j2} which give an information about the curvature according to the norm and the direction of the tangent vectors $\overrightarrow{P_{j0}P_{j1}}$ and $\overrightarrow{P_{j2}P_{j3}}$ (Figure 5a). The continuity between two consecutive curves is provided by identical upward and downward derivatives at each junction point. For each curve, P_{j0} and P_{j3} are referred to as anchor Bézier points. The anchor Bézier points are the set of model parameters $\mathbf{m}$. The junction points are anchor Bézier points which are common to two consecutive curves. Changing the position of junction points influences the shape of two consecutive curves. Therefore, the use of more than two Bézier curves is needed to depict independent variations with depth. This parameterization offers the advantage to describe both smooth and sharp variations with a minimum number of parameters (see Figure 5b for example of V_S profiles described using 6 and 4 anchor Bézier points) .

The range of possible velocity values is restricted by setting upper and lower velocity bounds (black lines in Figure 6a,b,c) based on the range of velocity values observed in the literature [Mooney et al., 1998; Shapiro & Ritzwoller, 2002]. A minimal distance of $dz = 10$ km is set between two consecutive anchor Bézier points in order to impose a more or less homogeneous distribution of anchor Bézier points with depth. The depth of each Bézier point can be freely taken within the first 100 km. At the top ($z = 0$ km) and the bottom ($z = 100$ km) the depths are set but V_S value can be randomly chosen within the prior. We force the presence of one anchor Bézier point at $z = 190$ km with velocity $V_S = 4.4$ km/s given by the PREM [Dziewonski & Anderson, 1981]. No other anchor point can exist in the $100 - 190$ km depth range. For each cubic Bézier curve, the associated control points which define the local tangents and ensure the continuity are set at a distance of 5 km from the corresponding anchor point. The amount of anchor Bézier points (hence the number of Bézier curves) varies according to each Markov chain, so that the model smoothness is made data adaptative, as in reversible jump McMC methods [Green, 1995].

3.2.3 Bayesian exploration

The fact that the *a priori* information $\rho_M(\mathbf{m})$ can not be described analytically and that each individual pdf in the data space may exhibit a complex shape with several maxima, a global search method must be used to solve the inverse problem. Therefore, we use a Monte-Carlo (MC) approach which does not assume any particular distribution and achieves a global search in the model space. Among others, Monte-Carlo approaches based on the Metropolis-Hastings (MH) algorithm [Metropolis & Ulam, 1949; Metropolis et al., 1953; Hastings, 1970] are widely used in geophysics [e.g. Tamminen & Kyrölä, 2001; Malinverno, 2002], especially in seismology [e.g. Bodin et al., 2012; Shen et al., 2013; Drilleau et al., 2013]. The MH algorithm is used in this study. The MH algorithm is an acceptance/rejection algorithm based on a likelihood ratio which designs a guided random walk in the model space that samples $\sigma(\mathbf{m})$. Each iteration involves a 3-steps process: (i) proposition, (ii) forward problem and likelihood computation and (iii) acceptance/rejection (Metropolis rule). (i) At the iteration j, a new model $\mathbf{m}_j$ is generated from a random perturbation of the previous one $\mathbf{m}_{j-1}$ following a proposal distribution $f(\mathbf{m}_j|\mathbf{m}_{j-1})$. The proposal distribution is often chosen to be symmetric and normally distributed, i.e $f(\mathbf{m}_j|\mathbf{m}_{j-1}) = \frac{1}{\gamma\sqrt{2\pi}}\exp(-(\mathbf{m}_j - \mathbf{m}_{j-1})^2/2\gamma^2)$ where γ is the standard deviation of the proposal distribution. (ii) The forward computation is done to enable the computation of the likelihood function $L(\mathbf{m}_j)$ associated with the proposed new model $\mathbf{m}_j$. (iii) The proposed model is accepted with the probability $P_a = \min[1\ ,\ L(\mathbf{m}_j)/L(\mathbf{m}_{j-1})]$. The Metropolis rule permits the acceptation of a model which deteriorates the likelihood value, avoiding the issue of converging to local minima. When the proposed model $\mathbf{m}_j$ is rejected, $\mathbf{m}_j = \mathbf{m}_{j-1}$ and thus $\mathbf{m}_{j-1}$ is sampled again. The resulting walk is called a Markov chain because each new sampled model only depends on the previous model. This Markov chain statisticially converge towards a unique equilibrium distribution that corresponds to the *a posteriori* pdf $\sigma(\mathbf{m})$, which is the solution to the inverse problem.

3.2.4 Practical implementation

A parallel 2-steps inversion scheme is proposed to speed-up the convergence towards the stationary period. During a first step that may be assigned to the burn-in period, a comprehensive exploration of the model space is performed by randomly perturbing the position of all anchor Bézier points using wide Gaussian proposal distributions. 16 independent Markov chains run in parallel with a different number of parameters ranging from 8 (5 anchor Bézier points) to 12 (8 anchor Bézier points). The 4 different parameter configurations are tested on 4 sets of 4 chains. The starting model for each chain is chosen randomly within the prior on parameters, and thus each chain follows different paths in the model space. Each chain runs over 10 000 iterations. The best-fitting model (largest likelihood value) is then determined for each chain. Based on a comparison of best fit values, an overall selection of 1/4 of the initial Markov chain amount is performed to start the second step. During the second step, 4 independent chains lasting 30 000 iterations each run in parallel. The sampling of the *a posteriori* pdf is thus provided by using the 4 best-fitting models retained at the end of the first step as starting models. At this stage the exploration is performed by modifying only one parameter (V_S or depth value) at each iteration. This is done with narrower Gaussian proposal distributions. The strategy ensures to preserve most of the characteristics of the current model, which may have resulted in a good data fit.

In this inversion scheme, various numbers of anchor Bézier points are tested in order not to *a priori* fix the smoothness of the sampled velocity profiles. Therefore, we fully benefit of the convenient property of Bayesian inference referred to as "natural parsimony", i.e. preference for the least complex explanation for an observation [MacKay, 2003], and in that sense, the algorithm shares some features with transdimensionnal inversion schemes [Green, 1995; Sambridge et al., 2012]. The group velocity dispersion curves are computed using the Thomson-Haskell method [Thomson, 1950; Haskell, 1953] in a non-attenuating spherical Earth [CPS Herrmann, 2013]. The Bézier curves are discretized into a set of homogeneous layers with a thickness of 2 km prior to the dispersion curve computation. The choice of 2 km allows to adequately describe both sharp and smooth variations that may exist in the Bézier curves. The choice of layer thickness has no influence on the number of model parameters. We only invert for V_S since Rayleigh waves group velocity dispersion measurement are much less sensitive to V_P and density than V_S [An & Assumpção, 2005]. Therefore, we use a constant V_P/V_S ratio of 1.73 to compute V_P, and we impose that density is 3000 kg/m^3 for z $\leq$ 45 km, and 4500 kg/m^3 below. The overall inversion scheme for one 1-D V_S profile takes about 10 min on a parallel computer system, for a total number of parameters inversed ranging from 8 to 12.

3.2.5 V_S *a posteriori pdfs*

Only the samples generated during the second step of the inversion are considered to be samples of the *a posteriori* pdf $\sigma(\mathbf{m})$. The first 5 000 samples of each chain are discarded to remove any dependence on the starting model. The remaining part of the chain is "thinned" by keeping 1 iteration over 2, in order to mitigate the covariance between models. Note that the use of several independent parallel Markov chains reduces the covariance between models. Finally, a total of 4×12 500 iterations are assembled together to build the *a posteriori* pdf, as the one presented in the Figure 6a. Next, we compute, for each station pair, a single velocity model with representative uncertainties at each depth. After several test and trials, we found that approximating the *a posteriori* pdf at each depth as a Gaussian pdf with mean and standard deviation taken from the 100 best fitting models (Figure 6c) is an acceptable choice because it allows us (i) to derive small uncertainties for unimodal well constrained inversion results in order to favor them in the subsequent tomographic procedure, (ii) to adequatly reflect the decrease of surface wave sensitivity with depth.

3.3 CLF-E089 station pair example

CLF-E089 is a NE-SW oriented station pair with an interstation distance of 980 km (see Figure 1b). The Figure 6 presents the results of the inversion of the empirical Green's function computed between the stations CLF and E089 (Figure 4a), once it has been converted into a Rayleigh wave group velocity pdfs dispersion diagram (Figure 4b). The group velocity pdfs dispersion diagram shown in Figure 4b is somehow noisy and exhibits some complexities, especially at short periods (5-8 s period band) where a bimodal distribution of the seismic energy is observed. The result of the McMC inversion is the *a posteriori* pdf computed from the accepted velocity model ensemble (Figure 6a). The *a posteriori* pdf shows smooth variations of the shear-wave velocity with depth. The *a posteriori* pdf is multimodal at shallow depths ($<$ 4 km) which directly reflects the data complexities at short periods. In contrast, the *a posteriori* pdf at greater depths is unimodal, and tends to be wider as the depth increases. This is the consequence of the decrease of the sensitivity of the surface wave with depth. The Figure 6d shows that the best fitting sampled models follow the main features of the data. In particular, the bimodal distribution of the seismic energy at short periods clearly appears as a broad distribution at short periods in Figure 6e. When looking at individual random velocity models (in blue in Figure 6b), it is clear that different families of velocity profiles exist at shallow depths. The standard deviation of the 100 best fitting models (Figure 6c) carry this pecularity by providing larger uncertainties in the 0-4 km depth range than in the 4-6 km depth range.

4 3-D V_S MODEL

4.1 Tomographic procedure

The tomographic procedure consists in the regionalization, at each depth, of the 1268 V_S values computed from the McMC inversion of each noise correlation dispersion diagram. The 3-D velocity model is constructed by gathering 2-D shear-wave velocity variations maps computed at each investigated depth from the regionalization. The regionalization used in this study is a local scale version of the CLASH [Beucler & Montagner, 2006] which has been initially developed for retrieving isotropic and anisotropic seismic velocity perturbations at global scales. The method proposed here relies on the following assumptions: (i) spherical Earth, (ii) ray theory, and (iii) great-circle approximation. Following Backus [1965], we express for the depth z the local azimuthally varying (angle Ψ) V_S perturbation at any point of latitude θ and longitude ϕ, as

$$\delta V(\theta,\phi,z,\Psi) = \frac{1}{2V_0(\theta,\phi,z)}\Big[A_1(\theta,\phi,z) + A_2(\theta,\phi,z)\cos 2\Psi + A_3(\theta,\phi,z)\sin 2\Psi + A_4(\theta,\phi,z)\cos 4\Psi + A_5(\theta,\phi,z)\sin 4\Psi\Big], \quad (3)$$

where $\delta V = V - V_0$. V_0 is a reference velocity (in our case given by the median of all path-averaged velocities). $A_1, \ldots, A_5$ depend on elastic parameters of the medium [Montagner & Nataf, 1986; Lévêque et al., 1998]. Following the conclusions of Trampert & Woodhouse

[2003] and Beucler & Montagner [2006], we include in the inversion process the isotropic term (A_1) and all the azimuthal anisotropic terms (i.e A_2, A_3, A_4, A_5) to prevent artefacts in the results. However, only the isotropic model will be discussed in this paper. The tomographic problem involves an iterative gradient least-squares optimization technique [Tarantola & Valette, 1982]. The question of which starting model to use at each depth has no trivial answer. Here, we choose as the starting model a uniform model with V_S value computed from the median of all the 1-D path average V_S values for a given depth. The model parameterization is based on 999 regularly spaced nodes every 50 km at the spherical Earth's surface. The relationship between the data and model parameters is directly governed by the ray path intersections. The inversion for $A_1, \ldots, A_5$ is controlled by three kinds of parameters : the *a priori* variance on data (β_d^2), the *a priori* variance on parameters (α_p^2) which constrains the anomaly amplitude, and the spatial correlation length (ℓ) which constrains the smoothness of the model parameters [Montagner, 1986]. Adequate ℓ values also ensure that all the model parameters are associated with a sufficient number of intersections between paths of various azimuths to solve the possible non-uniqueness induced by an uneven or an insufficient ray path coverage. Since the theoretical errors are assumed to be negligible, β_d corresponds, for a given station pair, to the *a posteriori* Gaussian standard deviation taken from the 100 best path average V_S velocity values retrieved from the McMC inversion of the corresponding noise cross-correlation dispersion diagram (Section 3). For each depth, the β_d^2 values are rescaled between 5% and 10%, and α_p^2 is set to 10% and 2% for the isotropic and the anisotropic components, respectively. The ℓ values for the isotropic and anisotropic terms are set to 75 km and 150 km, respectively. These values do not vary with depth because the path coverage is identical for each depth.

4.2 Resolution analysis

The synthetic reconstruction tests are an easy and fast method to gain insight into the resolution of the tomographic images. The use of tightly spaced checkerboard test is a common practice in ambient noise surface-wave tomography. However, as shown by Lévêque et al. [1993], this method can be misleading because small-size structures may be well retrieved while larger structures are not. Here, we follow the conclusions of Rawlinson & Spakman [2016] who advocate the use of a synthetic model involving a sparse distribution of spikes. The Figure 7a shows an example of such model. Each spike is a 100×100 km uniform isotropic velocity perturbations of +/- 10% with respect to the median velocity value. The synthetic data are calculated using the same forward problem and path coverage as available for real data analysis. The *a priori* variance (β_d^2) on synthetic data is taken from the real data inversion results for the depth of 30 km. The same inversion parameters as described in 4.1 are used. The only difference is that the azimuthal anisotropy is not taken into account. Figure 7b displays the retrieved model. The shape and the amplitude of the spikes located inland and along the shore in Brittany are well recovered. The slight blurring effect and the amplitude dampening are likely due to the spatial correlation between model parameters imposed by the tomography procedure. On the other hand, the spike located offshore in the Bay of Biscay is not well resolved. The output model exhibits a strong NE-SW stretching of the input anomaly, which may be clearly related to the poor azimuthal and intersection path coverage in this area, as shown in the Figure 7c,d.

4.3 3-D V_S model

The Figure 8a,b,c shows the inversion results at 4, 16, and 30 km depths, respectively. Each depth slice displays local perturbations of the isotropic V_S value with respect to the median V_S value for each depth (indicated in the lower right of each map). The inversion results display smooth lateral velocity variation in the resolved area, and the velocity perturbations are null outside the seismic network, which tends to show that developments to use the CLASH at local scale work. The results become more "patchy" at the border of the seismic network, especially in the Bay of Biscay where numerous small-scale perturbations are visible. Those small-scale perturbations are a logical consequence of the poor path coverage in these regions. The Figure 8d displays the *a posteriori* variance on the isotropic parameters computed for the 30 km depth slice result. The *a posteriori* variance is lower than to 5% in the resolved area, hence demonstrating the reliability of the results. The *a posteriori* variance map barely changes with depth since it is mainly controlled by the path coverage (Figure 7c), which remains identical for each depth in our case. At 4 km depth (Figure 8a), we observe a large scale "V-shape" positive perturbation across France. This strong (+4%) perturbation is centered in the Massif Central, and its westernward and easternward extensions cover the Armorican Massif and the Morvan, respectively. Small scale positive perturbations of weaker amplitude (+4%) are observed in Vosges, Foret Noire, Belgium, southwestern part of Great Britain (Cornwall), in the Iberian moutains, in the Alps, and in the eastermost part of the Pyrenees. Strong negative V_S perturbations (-7.5%) are found in the southwestern France, Bay of Biscay, southeastern France, and northern Spain. The model exhibits weaker negative perturbations (-2.5%) in the southern part of Great Britain, and in the center and northern part of France. At 16 km depth (Figure 8b), the velocity structure shows significant differences. The 16 km depth slice displays a large scale strong negative perturbation (-10%) over northwestern part of France. The southwestern part of France exhibits a moderate negative velocity perturbation (-5%). A localized strong (+10%) positive anomaly is observed in the Bay of Biscay. The eastern part of France is characterized by a moderate (+5%) positive North-South oriented velocity perturbation centered in the Massif Central. The 30 km depth slice (Figure 8d) exhibits similarities with the results obtained at 16 km, but the V_S perturbations are higher (+/-15%). Central France displays a strong negative (-15%) anomaly. The Bay of Biscay and surrounding regions is characterized by a large scale positive velocity perturbation, which includes the northeastern part of Spain, westernmost part of Brittany, and Cornwall. Moreover, the N-S oriented positive velocity perturbation in southeastern France detected at 16 km depth persists and covers a broader area. This velocity perturbation pattern is observed over the entire Massif Central and it extends further East across the Vosges-Black Forest regions.

5 DISCUSSION

The most obvious characteristic of the results at 4 km depth (Figure 8a) is the very good correlation of the V_S perturbations with the surface geology (see Figure 1a for details concerning geological region names). Indeed, the crystalline variscan massifs (Armorican Massif, Massif Central, Morvan, the Ardennes Massif, the Vosges, Black-Forest, Cornwall, Iberian mountains) are characterized by positive V_S perturbations, whereas Mesocenozoic sedimentary basins of France (Aquitan, Southeastern, and Paris basins), Great-Britain (Hampshire Weald basins) and Spain (Basque-Cantabrian, Ebro, and Duero basins) are associated with negative V_S perturbations. Our tomographic results delineates the same geological domains as recent absorption tomography results computed in the 1-2 Hz frequency range [Mayor et al., 2017]. Interestingly, the strongest signals (-7.5%) are located in the Southeastern basin, in the Basque-Cantabrian basin, and in the southern part of the Aquitan basin where the sediment depth is greater than 10 km [Fernandez-Mendiola & García-Mondejar, 1990; Le Pichon et al., 2010], and where persistent high attenuation regions have been detected by Mayor et al. [2017]. In contrast, weaker negative V_S perturbations (-2.5%) are observed in the Paris, Ebro, Duero, Hampshire and Weald basins, and the northern part of the Aquitan basin where the sediment filling does not exceed 4 km. In Figure 9a, we focus on the results at 4 km depth in western France and surrounding regions, after converting the V_S perturbations into absolute V_S values. Let us assume that $Vs < 3.15$ km/s are associated with Mesocenozoic sedimentary rocks (red-orange colors), and that $3.26 < V_S < 4.1$ km/s characterize crystaline rocks belonging to the pre-Mesozoic basement (green colors). Following this hypothesis, our results show that the connection between the South-Armorican domain and the Massif Central Variscan basement is made beneath the Poitou-High along a NW-SE oriented pattern (labelled as “PH” in Figure 9a). This result is in agreement with geodynamical models and observations showing that Variscan lithologies of the southern part of the Armorican Massif and the Massif Central are closely related, with a geometry that follows the NW-SE trend of the South-Armorican Shear Zone [e.g. Baptiste et al., 2016]. The V_S map also shows that the sediment column thickness might reach 4 km in the eastern part of the Paris basin ("E" label). This is in agreement with the assymetry of the sediment filling of the Paris basin, which is characterized by a higher sediment thickness in its eastern part [Perrodon & Zabek, 1990].

At 30 km depth, the tomographic image shows clearly different patterns (Figure 8c). The positive velocity perturbations in the Bay of Biscay and in the Vosges/Massif-Central/Southeastern part of France are most likely related to the presence of mantellic material. It is known that the Moho is shallow (< 20 km) beneath the Parentis basin, in the heart of the Bay of Biscay [Pinet & Montadert, 1987]. Our results also show that the Moho depth would not exceed 30 km beneath the Armorican and Cantabria shelfs, and that the ocean-continent transition would be located along the French and Spanish Atlantic coastlines. In the Vosges/Massif-Central/Southeastern part of France, our results show a thin crust, in agreement with the recent results of Macquet et al. [2014] and Chevrot et al. [2014]. Those regions would have experienced crustal thinning due to the Alpine orogeny [Autran et al., 1994]. On the contrary, the negative anomaly observed in center and northwestern parts of France could be related to a crustal thickening. In Figure 9b, we focus on the results at 30 km depth in western France and surrounding regions, after converting the V_S perturbations into absolute V_S values. Let us assume that $3.8 < V_S < 3.9$ km/s are associated with lower crust material, and that $V_S > 4.1$ km/s characterize mantellic rock. Following this hypothesis, our results show 4 regions of crustal material covering a large area in the northwestern part of France (labelled as "Z1", "Z2", "Z3", "Z4" in Figure 9b). This low velocity area seems to be limited in the East by the Paris Basin Magnetic Anomaly (PBMA) (eastern boundaries of "Z3" and "Z4") and in the South by the South-Armorican Shear Zone (SASZ) (southern boundaries of "Z2" and "Z3"). In the Armorican Massif, the southern boundary of this low velocity area follows the northern branch of the SASZ (southern boundary of "Z2"). Further East, this low velocity area is limited to the South by the southern branch of the SASZ and by the Nort-sur-Erdre (NSE) fault (southern boundary of "Z3"). The northward extension of this area is less clear, but it could be limited by the Rheic suture (northern boundaries of "Z1", "Z2" and "Z4"). The region "Z2" crosses the Central-Armorican domain in a vicinity of a zone where strong seismic attenuation and anomalous reflectivity pattern have been revealed by Campillo & Plantet [1991] and Matte & Hirn [1988], respectively. The vertical cross-section shown in Figure 9c, along with the Moho depths detected on the ECORS seismic profile from either side of this area [Matte & Hirn, 1988] supports the hypothesis of crustal thickening. Following the geodynamical models proposed by Ballèvre et al. [2009], the large area encompassing "Z1", "Z2", "Z3" and "Z4" could be associated with the deep crustal root of the Armorica microplate whose southern and eastern boundaries are the SASZ and the PBMA, respectively. Therefore, our results are in line with the hypothesis that both SASZ and the PBMA are major crustal boundaries which could be related to Variscan sutures. However, the presence in our tomographic model of two high velocity area in northwestern France (labels "L" and "Q") are more difficult to interpret. The "L" area covers the westernmost part of the Central- and North-Armorican domain, and its eastern boundary does not follow a known discontinuity. We speculate that this high velocity domain could be related to the Léon Domain, which is interpreted as a microcontinent in some geodynamical models [Ballèvre et al., 2009; Faure et al., 2010], but further investigations are needed to confirm this hypothesis. The "Q" area, which is located in the easternmost part of the North-Armorican domain and connected with high velocity area in southern Great-Britain, does not correlate, to the best of our knowledge, with a documented feature. Interestingly, the vertical cross-section shown in Figure 9c indicates that this area is associated with high velocities down to the mantle. Finally, we note that there is no evidence for a seismic signature of the Sillon Houiller which can sometimes be interpreted as a sharp boundary between lithospheric domains.

6 CONCLUSION

The analysis of 2 years of continuous seismic signals recorded at 55 broad-band stations located in France and in the surrounding countries allowed us to perform the first 3-D crustal regional V_S tomography focused on the western France and surrounding regions. The 1-D V_S variations with depth are computed from the inversion of Rayleigh wave ambient noise cross-correlation waveform, once it is converted into probability density functions of Rayleigh wave group velocity dispersion. A Markov chain Monte-Carlo inversion procedure allows to infer a posterior probability of V_S profiles which are turned into a mean 1-D path averaged V_S model with standard deviation. This depth inversion strategy has the advantage of not requiring group velocity dispersion picking, and to provide meaningful uncertainties of the V_S with depth. The data coverage enables to compute tomographic image with an unprecedented lateral resolution of 75 km over western France. The isotropic V_S maps correlate well with the geology at 4 km depth. While negative V_S anomalies are associated with the Mesocenozoic sedimentary basins, the crystalline Variscan basement displays positive anomalies. At greater depths, the Bay of Biscay exhibits positive V_S anomalies, whose eastern boundaries can be interpreted as the ocean-continent transition. The overall crustal structure below the Armorican Massif appears to be heterogenous at the subregional scale, and tends to support that both the South-Armorican Shear Zone and the Paris Basin Magnetic Anomaly are major crustal discontinuities that separate distinct domains. This 3-D crustal V_S model provides a new insight of crustal structure below western France and surrounding regions that could be incorporated in future seismotectonic zoning scheme of France for seismic hazard evaluation. Moreover, this model will contribute to better understand the moderate and diffuse seismicity over the Armorican Massif through an improved determination of earthquake hypocentral parameters that will take into account 3-D propagation effects. Future works include the analysis of azimuthal anisotropic terms, which could bring further insights about the structure at depth. In the near future, the tomographic model presented in this paper will be refined using data from recently installed permanent broad-band stations in western France (26 high quality permanent broad-band seismic stations since PYROPE experiment) which are deployed in the framework of the ongoing RESIF-CLB project. The RESIF-CLB project, which aims to build a permanent antenna of 200 broad-band stations deployed homogeneously over the metropolitan France will certainly allow to improve the knowledge of the deep structures beneath France.

ACKNOWLEDGEMENTS

This work is supported by the VIBRIS project (Council of Pays de la Loire), the ANR-09-0229-000 PYROPE project [Chevrot & Sylvander, 2017], and by the observatory of Nantes (OSUNA). The temporary experiment datasets are referred as DOI:10.15778/RESIF.X72010 and DOI:10.7914/SN/IB. The authors thank Olivier Quillard and Pierrick Gernignon for the installation and maintenance of the seismic stations in western France. The authors would like to thank Sébastien Chevrot, Mathieu Sylvander and all the PYROPE working group. We thank Mario Ruiz for preparing and providing IBERARRAY data. IBERARRAY is a contribution of the Team Consolider-Ingenio 2010 TOPO-IBERIA(CSD2006-00041) [Institute Earth Sciences "Jaume Almera" CSIC , ICTJA]. Data from the french permanent stations are freely available through the RESIF data portal (http://www.resif.fr). The authors would like to thank Sergei Lebedev for providing continuous records from the irish stations. The authors thank Thomas Bodin, Valérie Maupin and Martin Schimmel for fruitful discussions. All figures were produced by the GMT graphic software [Wessel et al., 2019]. Seismological data processing have been mainly done using the ObsPy library [Beyreuther et al., 2010] and SAC program [Goldstein & Snoke, 2005]. We thank Petr Kolínský for his very constructive and careful review. Constructive remarks by L. Boschi and an anonymous reviewer also helped improving this manuscript.

References

An, M. & Assumpção, M. S., 2005. Effect of lateral variation and model parameterization on surface wave dispersion inversion to estimate the average shallow structure in the Paraná Basin, *Journal of Seismology*, **9**(4), 449–462.

Arroucau, P., Mocquet, A., & Vacher, P., 2006. Atténuation de l'intensité macrosismique pour la France métropolitaine : importance de l'intensité épicentrale, *Comptes Rendus Géoscience*, **338**(9), 596 – 605.

Autran, A., Lefort, J., Debeglia, N., Edel, J., & Vigneresse, J., 1994. Gravity and magnetic expression of terranes in France and their correlation beneath overstep sequences, in *Pre-Mesozoic Geology in France and Related Areas*, pp. 49–72, ed. Keppie, J., Springer Berlin Heidelberg.

Backus, G. E., 1965. Possible forms of seismic anisotropy of the uppermost mantle under oceans, *Journal of Geophysical Research*, **70**(14), 3429–3439.

Ballèvre, M., Bosse, V., Ducassou, C., & Pitra, P., 2009. Palaeozoic history of the Armorican Massif: Models for the tectonic evolution of the suture zones, *Comptes Rendus Géoscience*, **341**(2–3), 174 – 201.

Baptiste, J., Martelet, G., Faure, M., Beccaletto, L., Reninger, P.-A., Perrin, J., & Chen, Y., 2016. Mapping of a buried basement combining aeromagnetic, gravity and petrophysical data: The substratum of southwest Paris Basin, France, *Tectonophysics*, **683**, 333–348.

Barmin, M. P., Ritzwoller, M. H., & Levshin, a. L., 2001. A fast and reliable method for surface wave tomography, *Pure and Applied Geophysics*, **158**(8), 1351–1375.

Bensen, G. D., Ritzwoller, M. H., Barmin, M. P., Levshin, a. L., Lin, F., Moschetti, M. P., Shapiro, N. M., & Yang, Y., 2007. Processing seismic ambient noise data to obtain reliable broad-band surface wave dispersion measurements, *Geophys. J. Int.*, **169**(3), 1239–1260.

Beucler, E. & Montagner, J.-P., 2006. Computation of Large Anisotropic Seismic Heterogeneities (CLASH), *Geophys. J. Int.*, **165**, 447–468.

Beucler, E., Mocquet, A., Schimmel, M., Chevrot, S., Quillard, O., Vergne, J., & Sylvander, M., 2015. Observation of deep water microseisms in the North Atlantic ocean using tide modulations, *Geophysical Research Letters*, **42**(2), 316–322, 2014GL062347.

Beyreuther, M., Barsch, R., Krischer, L., Megies, T., Behr, Y., & Wassermann, J., 2010. ObsPy: A Python Toolbox for Seismology, *Seismological Research Letters*, **81**(3), 530–533.

Bitri, A., Brun, J. P., Truffert, C., & Guennoc, P., 2001. Deep seismic imaging of the

Cadomian thrust wedge of Northern Brittany, *Tectonophysics*, **331**(1-2), 65–80.

Bitri, A., Ballèvre, M., Brun, J.-P., Chantraine, J., Gapais, D., Guennoc, P., Gumiaux, C., & Truffert, C., 2003. Imagerie sismique de la zone de collision hercynienne dans le Sud-Est du Massif armoricain (projet Armor 2/programme Géofrance 3D), *Comptes Rendus Géoscience*, **335**(13), 969–979.

Bitri, A., Brun, J.-P., Gapais, D., Cagnard, F., Gumiaux, C., Chantraine, J., Martelet, G., & Truffert, C., 2010. Deep reflection seismic imaging of the internal zone of the South Armorican Hercynian belt (western France) (ARMOR 2/Géofrance 3D Program), *Comptes Rendus Géoscience*, **342**(6), 448–452.

Bodin, T., Sambridge, M., Tkalčić, H., Arroucau, P., Gallagher, K., & Rawlinson, N., 2012. Transdimensional inversion of receiver functions and surface wave dispersion, *Journal of Geophysical Research*, **117**(B2), B02301.

Bois, C., Sibuet, J.-C., & Gariel, O., 1991. Etude de la croûte terrestre par sismique profonde; mer celtique-manche et ses approches occidentales; profils SWAT et WAM., *Mémoires de la Société Gólogique de France, Nouvelle Śrie*, **159**(1).

Campillo, M., 2006. Phase and Correlation in 'Random' Seismic Fields and the Reconstruction of the Green Function, *Pure and Applied Geophysics*, **163**(2-3), 475–502.

Campillo, M. & Paul, A., 2003. Long-range correlations in the diffuse seismic coda, *Science*, **299**(5606), 547–9.

Campillo, M. & Plantet, J., 1991. Frequency dependence and spatial distribution of seismic attenuation in France: experimental results and possible interpretations, *Physics of the Earth and Planetary Interiors*, **67**(1), 48–64.

Cauchie, L. & Saccorotti, G., 2012. Probabilistic inversion of Rayleigh wave dispersion data: an application to Mt Etna, Italy, *Journal of Seismology*, **17**(2), 335–346.

Cazes, M., Torreilles, G., Bois, C., Damotte, B., Galdeano, A., Hirn, A., Mascle, A., Matte, P., Van Ngoc, P., & Raoult, J. F., 1985. Structure de la croûte hercynienne du nord de la France; premiers résultats du profil ECORS, *Bulletin de la Societe Geologique de France*, **I**(6), 925–941.

Cazes, M., Mascle, A., Torreilles, X., Bois, C., Damotte, X., Matte, P., Raoult, X., Pham, V. N., Hirn, A., & Galdeano, X., 1986. Large Variscan overthrusts beneath the Paris Basin, *Nature*, **323**(6084), 144–147.

Chantraine, J., Autran, A., & Cavelier, C., 2003. Carte géologique de France au millionième, 6ième éd. révisée brgm, BRGM.

Chevrot, S. & Sylvander, M., 2017. Seismic network X7: PYROPE, PYRenean Observational Portable Experiment (RESIF-SISMOB),RESIF - Réseau sismologique et géodésique français, 10.15778/resif.x72010, https://doi.org/10.15778/resif.x72010.

Chevrot, S., Sylvander, M., Benahmed, S., Ponsolles, C., Lefèvre, J. M., & Paradis, D., 2007. Source locations of secondary microseisms in western Europe: Evidence for both coastal and pelagic sources, *Journal of Geophysical Research*, **112**(B11), B11301.

Chevrot, S., Villasenor, A., Sylvander, M., Benahmed, S., Beucler, E., Cougoulat, G., Delmas, P., de Saint Blanquat, M., Diaz, J., Gallart, J., Grimaud, F., Lagabrielle, Y., Manatschal, G., Mocquet, A., Pauchet, H., Paul, A., Péquegnat, C., Quillard, O., Roussel, S., Ruiz, M., & Wolyniec, D., 2014. High-resolution imaging of the Pyrenees and Massif Central from the data of the PYROPE and IBERARRAY portable array deployments, *Journal of Geophysical Research: Solid Earth*, **119**(8), 6399–6420.

Cloetingh, S., Burov, E., Matenco, L., Beekman, F., Roure, F., & Ziegler, P. A., 2013. The moho in extensional tectonic settings: Insights from thermo-mechanical models, *Tectonophysics*, **609**, 558–604, Moho: 100 years after Andrija Mohorovicic.

Diaz, J., Villasenor, A., Gallart, J., Morales, J., Pazos, A., Córdoba-Barba, D., Pulgar, J., García-Lobón, J., & Harnafi, M., 2009. The IBERARRAY broadband seismic network: A new tool to investigate the deep structure beneath Iberia, *Orfeus Newsl*, **8**.

D'Lemos, R. S., Strachan, R. A., & Topley, C. G., 1990. The Cadomian orogeny in the North Armorican Massif: A brief review, *Geological Society, London, Special Publications*, **51**(1), 3–12.

Drilleau, M., Beucler, E., Mocquet, A., Verhoeven, O., Moebs, G., Burgos, G., Montagner, J.-P., & Vacher, P., 2013. A Bayesian approach to infer radial models of temperature and anisotropy in the transition zone from surface wave dispersion curves, *Geophys. J. Int.*, **195**(2), 1165–1183.

Dziewonski, A. M. & Anderson, D. L., 1981. Preliminary Reference Earth Model, *Physics of the Earth and Planetary Interiors*, **25**(4), 297 – 356.

Ekström, G., 2011. A global model of Love and Rayleigh surface wave dispersion and anisotropy, 25-250 s, *Geophys. J. Int.*, **187**(3), 1668–1686.

Ermert, L., Villaseñor, A., & Fichtner, A., 2015. Cross-correlation imaging of ambient noise sources, *Geophys. J. Int.*, **204**(1), 347–364.

Faure, M., Sommers, C., Melleton, J., Cocherie, A., & Lautout, O., 2010. The Léon Domain (French Massif Armoricain): A westward extension of the Mid-German Crystalline Rise? Structural and geochronological insights, *International Journal of Earth Sciences*, **99**(1), 65–81.

Fernandez-Mendiola, P. & García-Mondejar, J., 1990. Mid-cretaceous palaeogeographical evolution of the central Basque-Cantabrian basin (northern Spain), *Palaeogeography, Palaeoclimatology, Palaeoecology*, **81**(1–2), 115 – 126.

Friedrich, A., Krüger, F., & Klinge, K., 1998. Ocean-generated microseismic noise located with the Gräfenberg array, *Journal of Seismology*, **2**(1), 47–64.

Gaudot, I., Beucler, E., Mocquet, A., Schimmel, M., & Le Feuvre, M., 2016. Statistical redundancy of instantaneous phases: Theory and application to the seismic ambient wavefield, *Geophys. J. Int.*, **204**(2), 1159–1163.

Goldstein, P. & Snoke, A., 2005. SAC Availability for the IRIS Community, *Incorporated Institutions for Seismology Data Management Center Electronic Newsletter*.

Green, P. J., 1995. Reversible jump Markov chain Monte Carlo computation and Bayesian model determination, *Biometrika*, **82**(4), 711.

Haskell, N. A., 1953. The dispersion of surface waves on multilayered media, *Bulletin of the Seismological Society of America*, **43**(1), 17–34.

Hastings, W. K., 1970. Monte Carlo sampling methods using Markov chains and their applications, *Biometrika*, **57**, 97˜109.

Herrmann, R. B., 2013. Computer Programs in Seismology: An evolving tool for instruction and research, *Seismological Research Letters*, **84**(6), 1081–1088.

Institute Earth Sciences “Jaume Almera” CSIC (ICTJA), S., 2007. IberArray: International Federation of Digital Seismograph Networks, 10.7914/sn/ib, http://iberarray.ictja.csic.es/.

Kolínský, P., Valenta, J., & Málek, J., 2014. Velocity model of the Hronov-Poříčí Fault Zone from Rayleigh wave dispersion, *J. Seismol.*, **18**, 617–635.

Kolínský, P., Bokelmann, G., & Group, A. W., 2019. Arrival angles of teleseismic fundamental mode Rayleigh waves across the AlpArray, *Geophys. J. Int.*, **218**, 114–144.

Le Pichon, X., Rangin, C., Hamon, Y., Loget, N., Lin, J. Y., Andreani, L., & Flotte, N., 2010. Geodynamics of the France Southeast basin, *Bulletin de la Société Géologique de France*, **181**(6), 477–501.

Lebedev, S., Nolet, G., Meier, T., & Van Der Hilst, R. D., 2005. Automated multimode inversion of surface and S waveforms, *Geophys. J. Int.*, **162**(3), 951–964.

Lévêque, J., Debayle, E., & Maupin, V., 1998. Anisotropy in the Indian ocean upper mantle from Rayleigh- and Love-waveform inversion, *Geophys. J. Int.*, **133**(3), 529–540.

Lévêque, J.-J., Rivera, L., & Wittlinger, G., 1993. On the use of the checker-board test to assess the resolution of tomographic inversions, *Geophys. J. Int.*, **115**(1), 313.

Levshin, a. L. & Ritzwoller, M. H., 2001. Automated detection, extraction, and measurement of regional surface waves, *Pure and Applied Geophysics*, **158**(8), 1531–1545.

Levshin, A. L., Yanovskaya, T., Lander, A., Bukchin, B., Barmin, M., L.I., R., & Its, E., 1989. Seismic surface waves in a laterally inhomogeneous Earth, *Modern Approaches in Geophysics*, **9**.

Lu, Y., Stehly, L., Paul, A., & Group, A. W., 2018. High-resolution surface wave tomography of the European crust and uppermost mantle from ambient seismic noise, *Geophysical Journal International*, **214**(2), 1136–1150.

MacKay, D. J. C., 2003. *Information Theory, Inference & Learning Algorithms*, Cambridge University Press, New York, NY, USA.

Macquet, M., Paul, A., Pedersen, H. A., Villasenor, A., Chevrot, S., Sylvander, M., & Wolyniec, D., 2014. Ambient noise tomography of the Pyrenees and the surrounding regions: inversion for a 3-D Vs model in the presence of a very heterogeneous crust, *Geophys. J. Int.*, **199**(1), 402–415.

Malinverno, A., 2002. Parsimonious Bayesian Markov chain Monte Carlo inversion in a nonlinear geophysical problem, *Geophys. J. Int.*, **151**(3), 675.

Martelet, G., Calcagno, P., Gumiaux, C., Truffert, C., Bitri, A., Gapais, D., & Brun, J., 2004. Integrated 3D geophysical and geological modelling of the Hercynian suture zone in the Champtoceaux area (south Brittany, France), *Tectonophysics*, **382**(1–2), 117 – 128.

Matte, P., 2001. The Variscan collage and orogeny (480–290 Ma) and the tectonic definition of the Armorica microplate: a review, *Terra Nova*, **13**(2), 122–128.

Matte, P. & Hirn, A., 1988. Seismic signature and tectonic cross section of the variscan crust in western France, *Tectonics*, **7**(2), 141–155.

Mayor, J., Traversa, P., Calvet, M., & Margerin, L., 2017. Tomography of crustal seismic attenuation in Metropolitan France: Implications for seismicity analysis, *Bulletin of Earthquake Engineering*, **16**(6), 2195–2210.

Metropolis, N. & Ulam, S. M., 1949. The Monte Carlo Method, *Journal of the American Statistical Association*, **44**(247), 335–341.

Metropolis, N., Rosenbluth, A. W., Rosenbluth, M. N., Teller, A. H., & Teller, E., 1953. Equation of state calculations by fast computing machines, *The Journal of Chemical Physics*, **21**(6), 1087–1092.

Montagner, J.-P., 1986. Regional three-dimensional structures using long-period surface waves, *Annales Geophysicae*, **4**, 283–294.

Montagner, J.-P. & Nataf, H.-C., 1986. A simple method for inverting the azimuthal anisotropy of surface waves, *Journal of Geophysical Research: Solid Earth*, **91**(B1), 511–520.

Mooney, W. D., Laske, G., & Masters, T. G., 1998. CRUST 5.1: A global crustal model at 5° × 5°, *Journal of Geophysical Research: Solid Earth*, **103**(B1), 727–747.

Nicolson, H., Curtis, a., & Baptie, B., 2014. Rayleigh wave tomography of the British Isles from ambient seismic noise, *Geophys. J. Int.*, **198**(2), 637–655.

Nishida, K., Montagner, J.-P., & Kawakatsu, H., 2009. Global surface wave tomography using seismic hum, *Science*, **326**(5949), 112–112.

Nolet, G., 1990. Partitionned waveform inversion and two-dimensional structure under the network of autonomously recording seismographs, *J. Geophys. Res.*, **95**, 8499–8512.

Panning, M. P., Beucler, E., Drilleau, M., Mocquet, A., Lognonné, P., & Banerdt, W. B., 2015. Verifying single-station seismic approaches using Earth-based data: Preparation for data return from the InSight mission to Mars, *Icarus*, **248**, 230–242.

Perrodon, A. & Zabek, J., 1990. Interior cratonic basins, chap. Paris Basin, pp. 633–679.

Pinet, B. & Montadert, L., 1987. Deep seismic reflection and refraction profiling along the Aquitaine shelf (Bay of Biscay), *Geophys. J. Int.*, pp. 305–312.

Rawlinson, N. & Spakman, W., 2016. On the use of sensitivity tests in seismic tomography, *Geophys. J. Int.*, **205**(2), 1221.

Ritzwoller, M. H. & Levshin, A. L., 1998. Eurasian surface wave tomography: group velocities, *Journal of Geophysical Research: Solid Earth*, **103**(B3), 4839–4878.

Sabra, K. G., Gerstoft, P., Roux, P., & Kuperman, W., 2005. Extracting time-domain Green's function estimates from ambient seismic noise, *Geophysical Research Letters*, **32**.

Sambridge, M., Bodin, T., Gallagher, K., & Tkalčić, H., 2012. Transdimensional inference in the geosciences, *Philosophical Transactions of the Royal Society of London A: Mathematical, Physical and Engineering Sciences*, **371**(1984).

Sapin, M. & Prodehl, C., 1973. Long range profiles in western Europe I.-Crustal structure between the Bretagne and the Central Massif, *Annales de Géophysique*, **358**, 127–145.

Shapiro, N. M. & Ritzwoller, M. H., 2002. Monte-Carlo inversion for a global shear-velocity model of the crust and upper mantle, *Geophys. J. Int.*, **151**(1), 88–105.

Shapiro, N. M., Campillo, M., Stehly, L., & Ritzwoller, M. H., 2005. High-resolution surface-wave tomography from ambient seismic noise, *Science*, **307**(5715), 1615–1618.

Shen, W., Ritzwoller, M. H., Schulte-Pelkum, V., & Lin, F.-C., 2013. Joint inversion of surface wave dispersion and receiver functions: a Bayesian Monte-Carlo approach, *Geophys. J. Int.*, **192**(2), 807–836.

Stehly, L., Campillo, M., & Shapiro, N. M., 2006. A study of the seismic noise from its long-range correlation properties, *Journal of Geophysical Research*, **111**(B10), B10306.

Tamminen, J. & Kyrölä, E., 2001. Bayesian solution for nonlinear and non-Gaussian inverse problems by Markov chain Monte Carlo method, *Journal of Geophysical Research: Atmospheres*, **106**(D13), 14377–14390.

Tarantola, A., 2005. *Inverse Problem Theory and Methods for Model Parameter Estimation*, Society for Industrial and Applied Mathematics, Philadelphia, PA, USA.

Tarantola, A. & Valette, B., 1982. Generalized nonlinear inverse problems solved using the least squares criterion, *Reviews of Geophysics*, **20**(2), 219–232.

Thomson, W. T., 1950. Transmission of elastic waves through a stratified solid medium, *Journal of Applied Geophysics*, **21**, 89–93.

Trampert, J. & Woodhouse, J. H., 2003. Global anisotropic phase velocity maps for fundamental mode surface waves between 40 and 150 s, *Geophys. J. Int.*, **154**(1), 154.

Verbeke, J., Boschi, L., Stehly, L., Kissling, E., & Michelini, a., 2012. High-resolution Rayleigh-wave velocity maps of central Europe from a dense ambient-noise data set, *Geophys. J. Int.*, **188**(3), 1173–1187.

Wessel, P., Luis, J. F., Uieda, L., Scharroo, R., Wobbe, F., Smith, W. H. F., & Tian, D., 2019. The generic mapping tools version 6, *Geochemistry, Geophysics, Geosystems*, **20**(11), 5556–5564.

Yang, Y. & Ritzwoller, M. H., 2008. Characteristics of ambient seismic noise as a source for surface wave tomography, *Geochemistry, Geophysics, Geosystems*, **9**(2).

Yang, Y., Ritzwoller, M. H., Levshin, A. L., & Shapiro, N. M., 2007. Ambient noise Rayleigh wave tomography across Europe, *Geophys. J. Int.l*, **168**(1), 259–274.

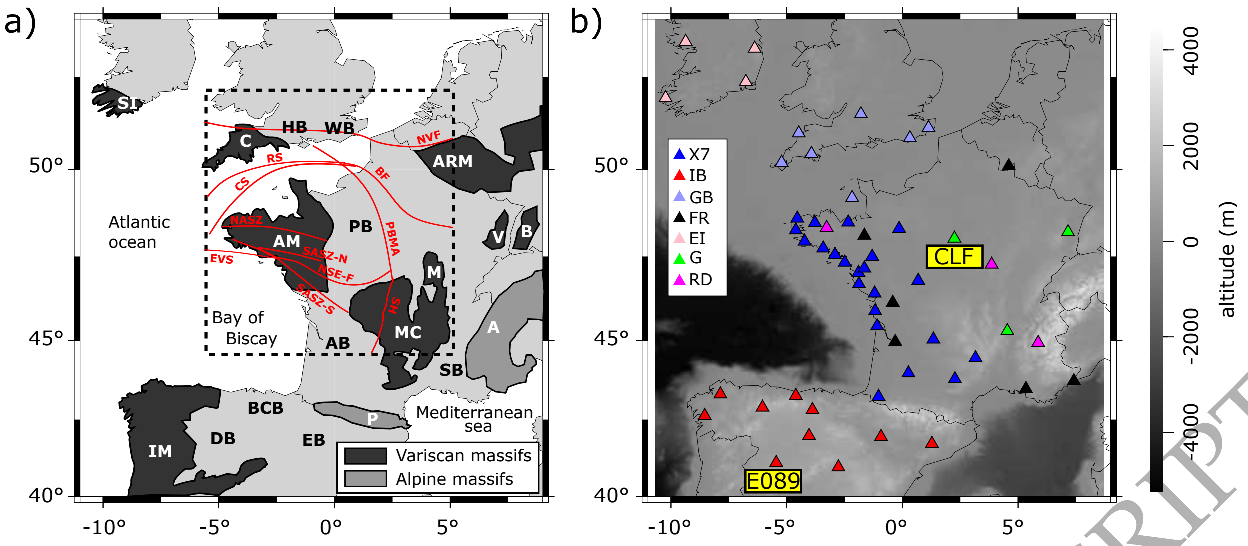

Figure 1. a) Map showing the main geological and structural features of the studied area after Chantraine et al. [2003] and Baptiste et al. [2016]. Crystalline basement (AM: Armorican Massif, MC: Massif Central, M: Morvan, IM: Iberian massif, SI: South Ireland, C: Cornwall, B: Black Forest, V: Vosges, ARM: Ardennes-Rhenish massif, P: Pyrenees, A: Alps), Mesocenozoic sedimentary basins (PB: Paris basin, AB: Aquitaine basin, SB: Southeastern basin, EB: Ebro basin, BCB: Basque-Cantabrian basin, DB: Duero basin, HB: Hampshire basin, WB: Weald basin). Structural features of the western France and surrounding regions (NASZ: North-Armorican Shear Zone, SASZ-N(S): Northern and Southern branch of the South-Armorican Shear Zone, NSE-F: Nort-sur-Erdre fault, EVS: Eo-Variscan suture, PBMA: Paris Basin Magnetic Anomaly, BF: Bray fault, SH: Sillon Houiller, NVF: North Variscan Front, CS: Le Conquet suture, RS: Rheic suture). The dashed black rectangle indicates the western France and the surrounding regions. b) Location of the 55 seismic broad-band stations used in this study. X7: PYROPE, IB: IBERARRAY, GB: Great-Britain, FR: RLBP, EI: Ireland, G: Geoscope, RD: CEA-LDG.

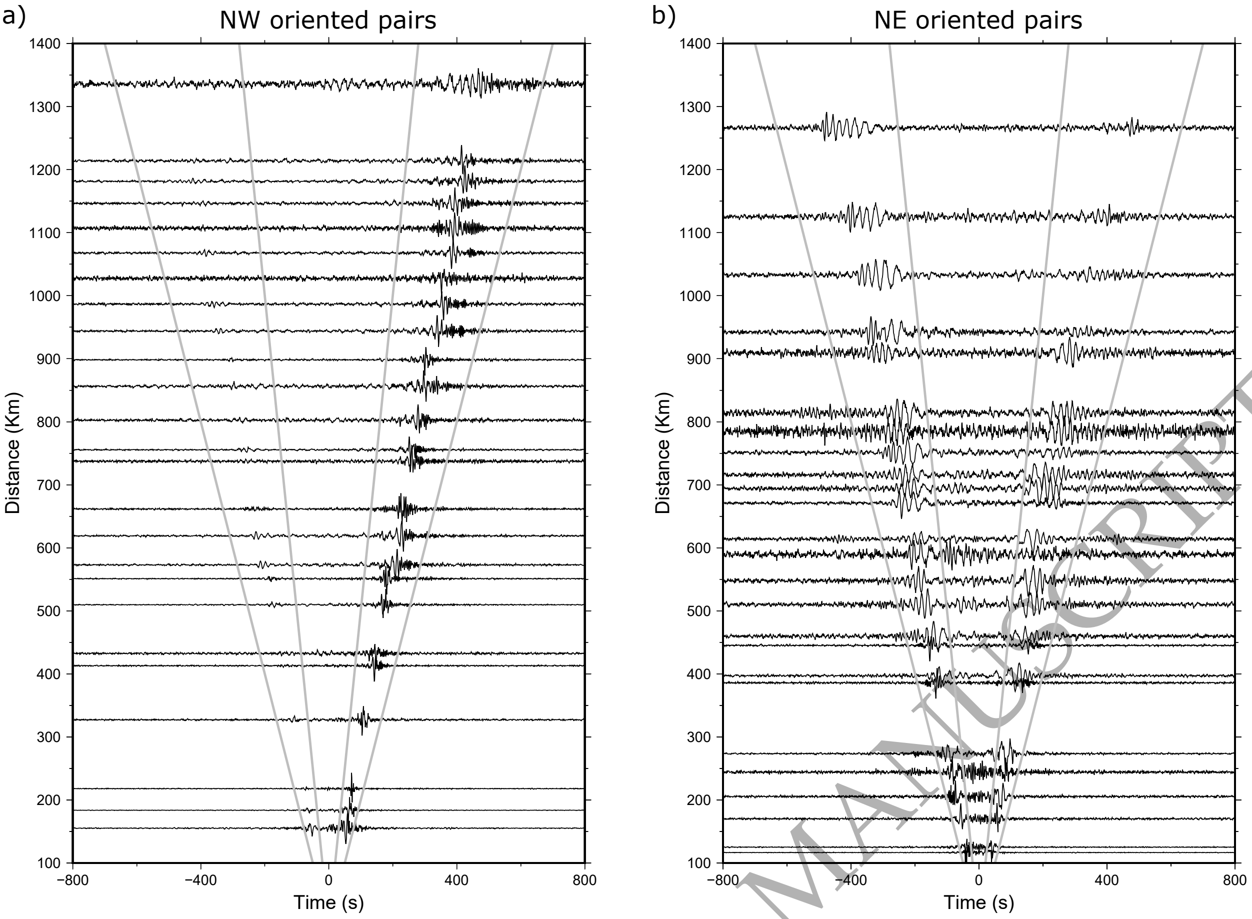

Figure 2. Cross-correlations filtered in the 2.5-50 s period band represented in time-distance plots. a) Subset of 25 cross-correlations from North-West ($N135° +/- 3.5°$) oriented pairs. The virtual source is the northermost station for each station pair, so that seismic energy propagating from northwest to southeast contributes to the signals in positive lags. b) Subset of 25 cross-correlations from North-East ($N45° +/- 3.5°$) oriented pairs. The virtual source is the westernmost station for each station pair, so that seismic energy propagating from southwest to northeast contributes to the signals in positive lags. The gray lines indicate linear move-outs of 2 km/s and 5 km/s. Clear emergent signals with a move-out near 3 km/s is observed. Each correlation is normalized relative to its absolute maximum.

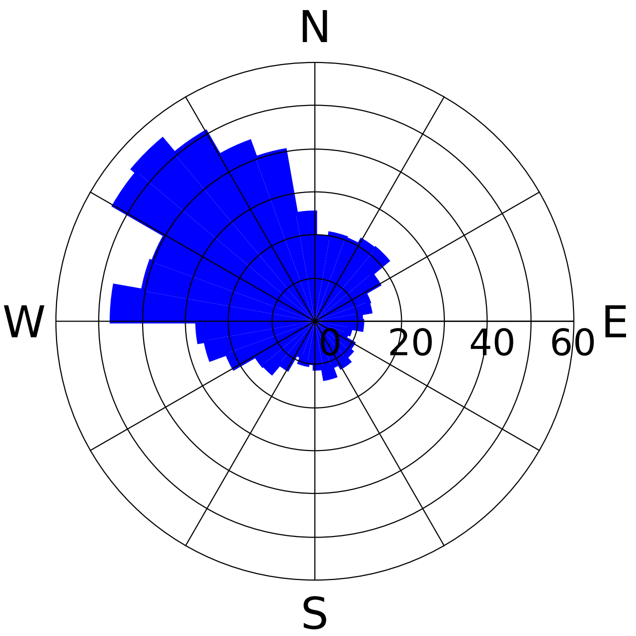

Figure 3. Azimuthal distribution of the signal-to-noise ratio (SNR) associated with the cross-correlations filtered in the 2.5-50 s period band (see Figure 2). The averages SNR values computed over bins of 10° are represented.

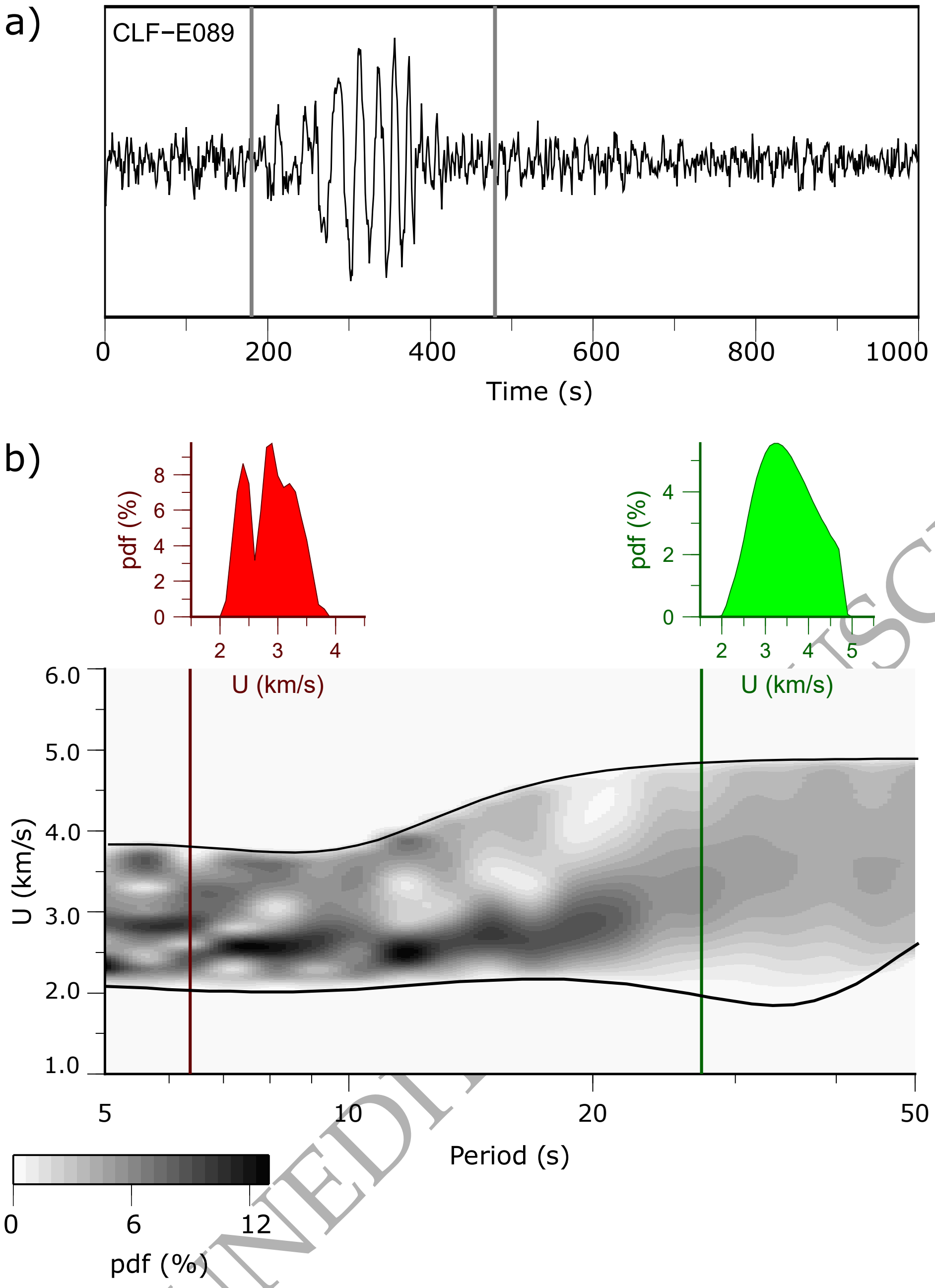

Figure 4. Dispersion diagram computation for CLF-E089 station pair. a) Symmetrized noise cross-correlation computed between CLF and E089 (see Figure 1b for stations locations). The gray lines indicate arrival times for waves propagating along the great circle interstation path with typical surface wave velocities of 2 km/s and 5 km/s. b) Dispersion diagram of the signal presented in a). At each period, the seismic energy is converted into an individual pdf of the seismic energy (see text for details). The pdfs associated with periods of 6.5 s and 28.5 s are shown above in red and green, respectively.

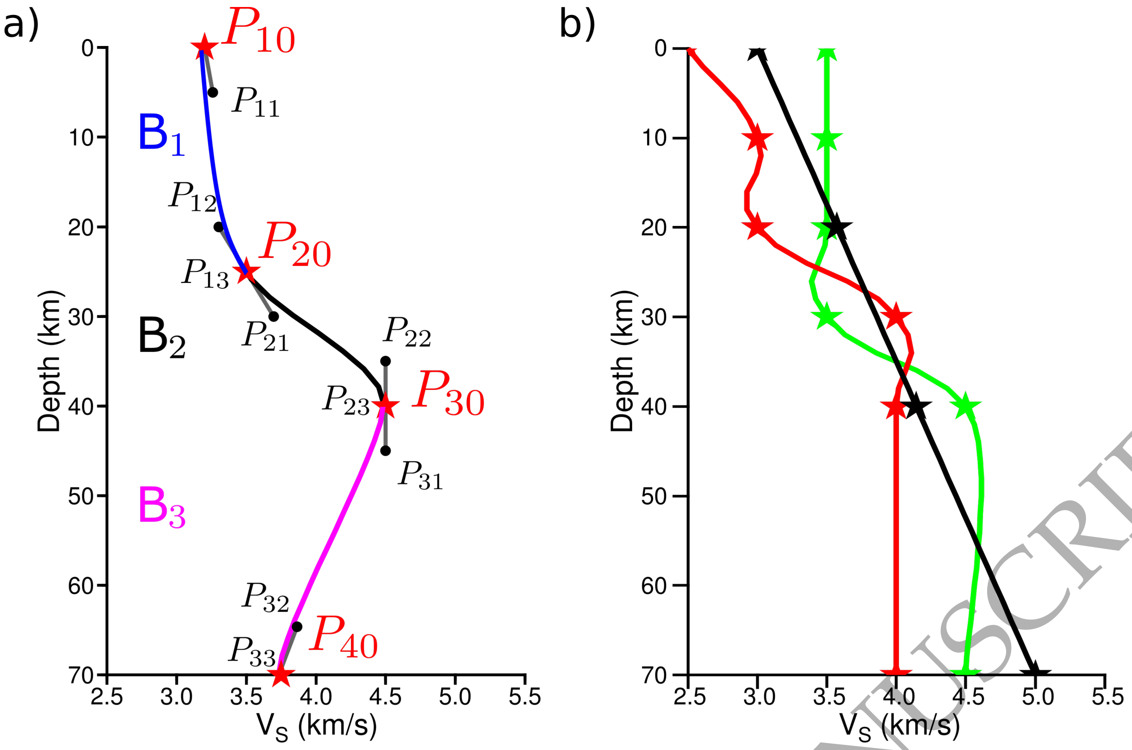

Figure 5. Bézier curve model parameterization. a) Sketch showing 3 Bézier curves in blue (B_1, top) , black (B_2, middle) , and magenta (B_3, bottom) . The anchor Bézier points are indicated with stars. Other control point and tangent vectors are indicated using black dots and gray segments, respectively. b) Example of three V_S profiles parameterized using 6 (red and green profiles) and 4 anchor Bézier points (black profile). The three V_S profiles satisfy the prior rule described in Section 3.2.2.

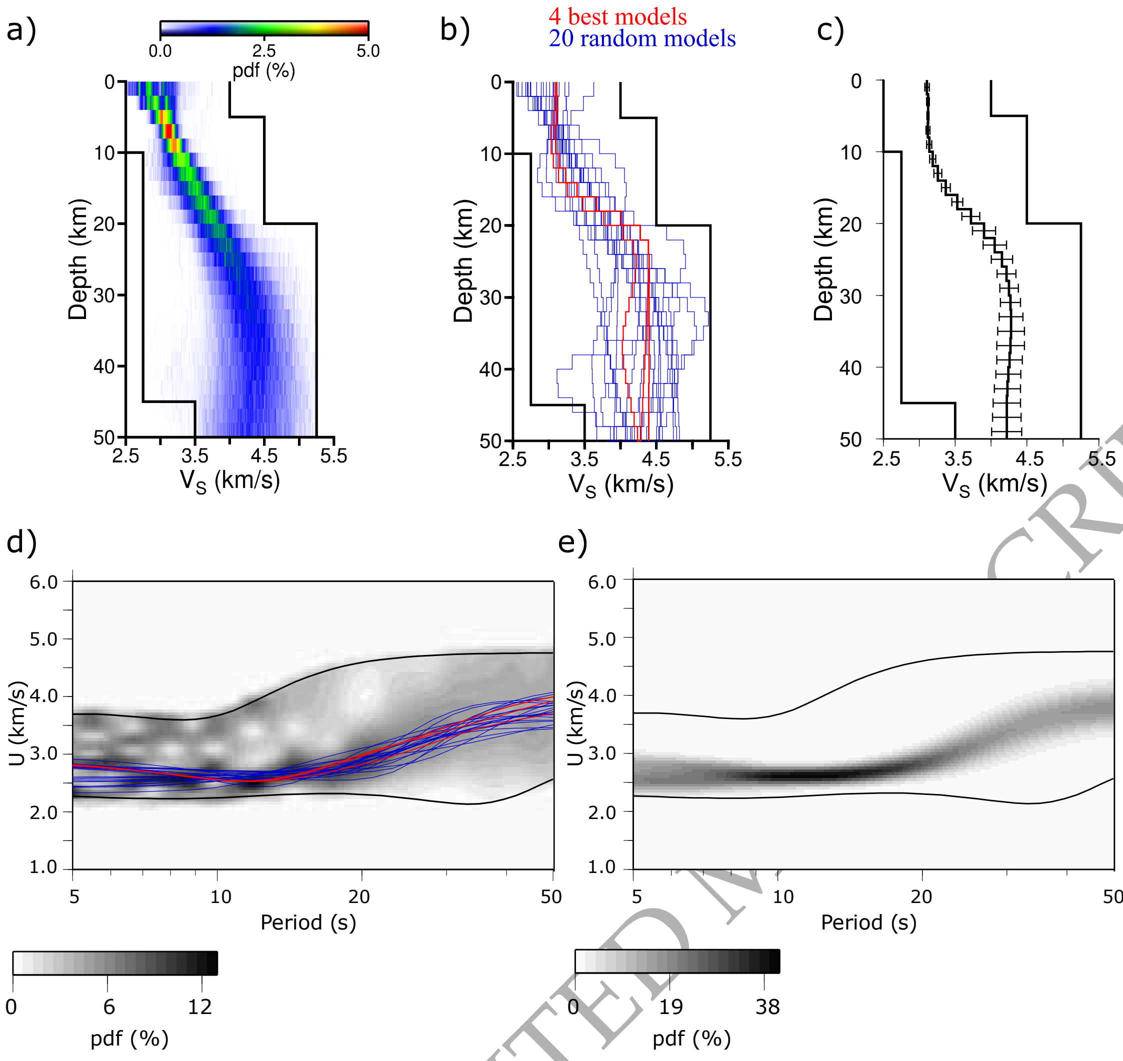

Figure 6. Monte-Carlo depth inversion results for the CLF-E089 station pair. a) *a posteriori* pdf from the accepted V_S model ensemble. b) 4 best (red) and 20 random (blue) V_S models. c) Mean and standard deviation of the 100 best V_S models. d) Dispersion diagram for CLF-E089 station pair. The group velocity dispersion curves associated with the 4 best and 20 random V_S models represented in b) are plotted in red and blue, respectively. e) Ensemble of the predicted group velocity dispersion curves associated with the accepted V_S models during the inversion procedure, represented in terms of pdf in the data space. In a,b,c, the vertical black lines represent the upper and lower bound V_S models, giving the minimum and maximum V_S values allowed at each depth.

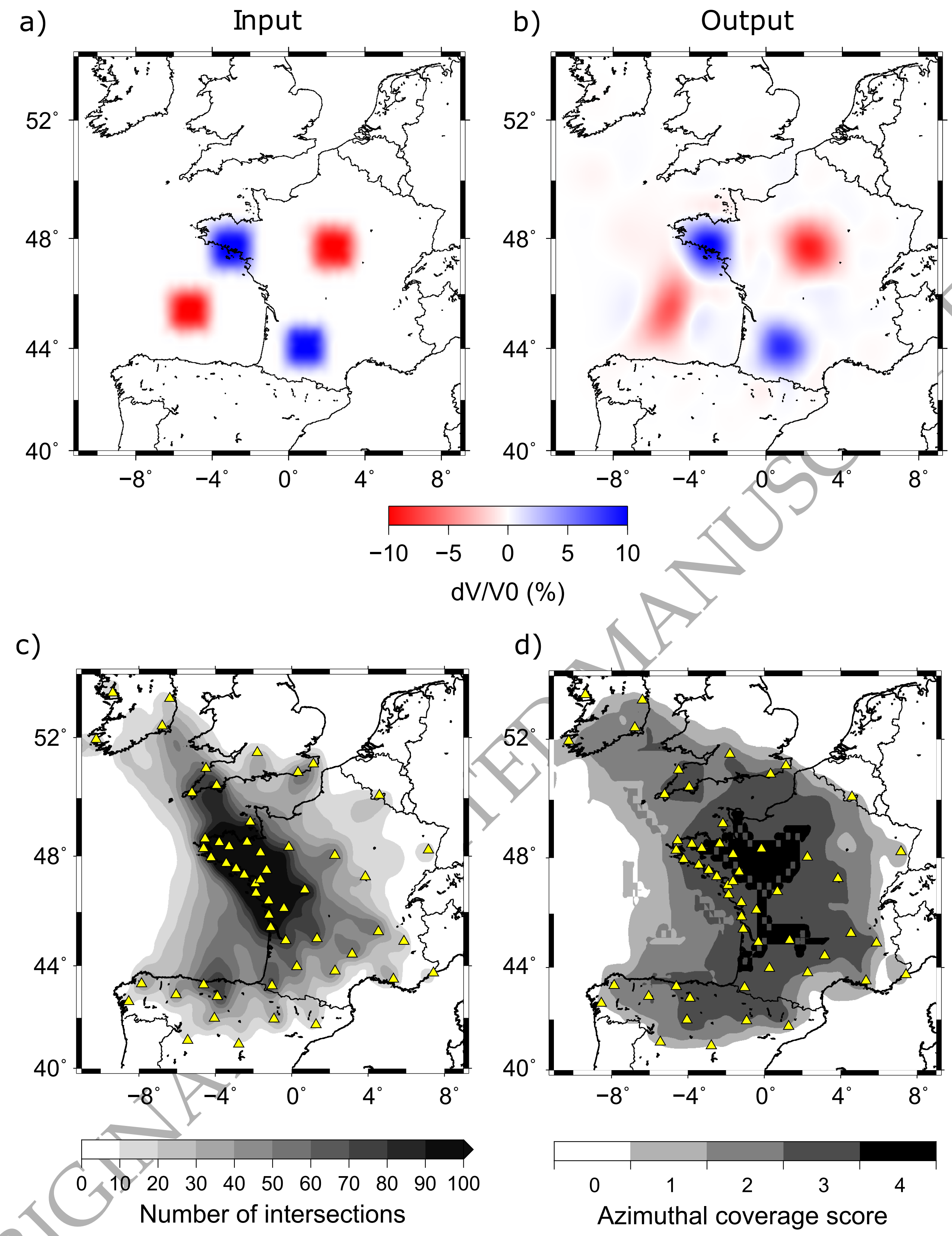

Figure 7. Resolution test and path coverage. a) Input model. b) Output model. c) Path coverage in terms of number of intersections. d) Path coverage in terms of azimuthal coverage score. A score of 4 indicates at least one path in the four quadrants.

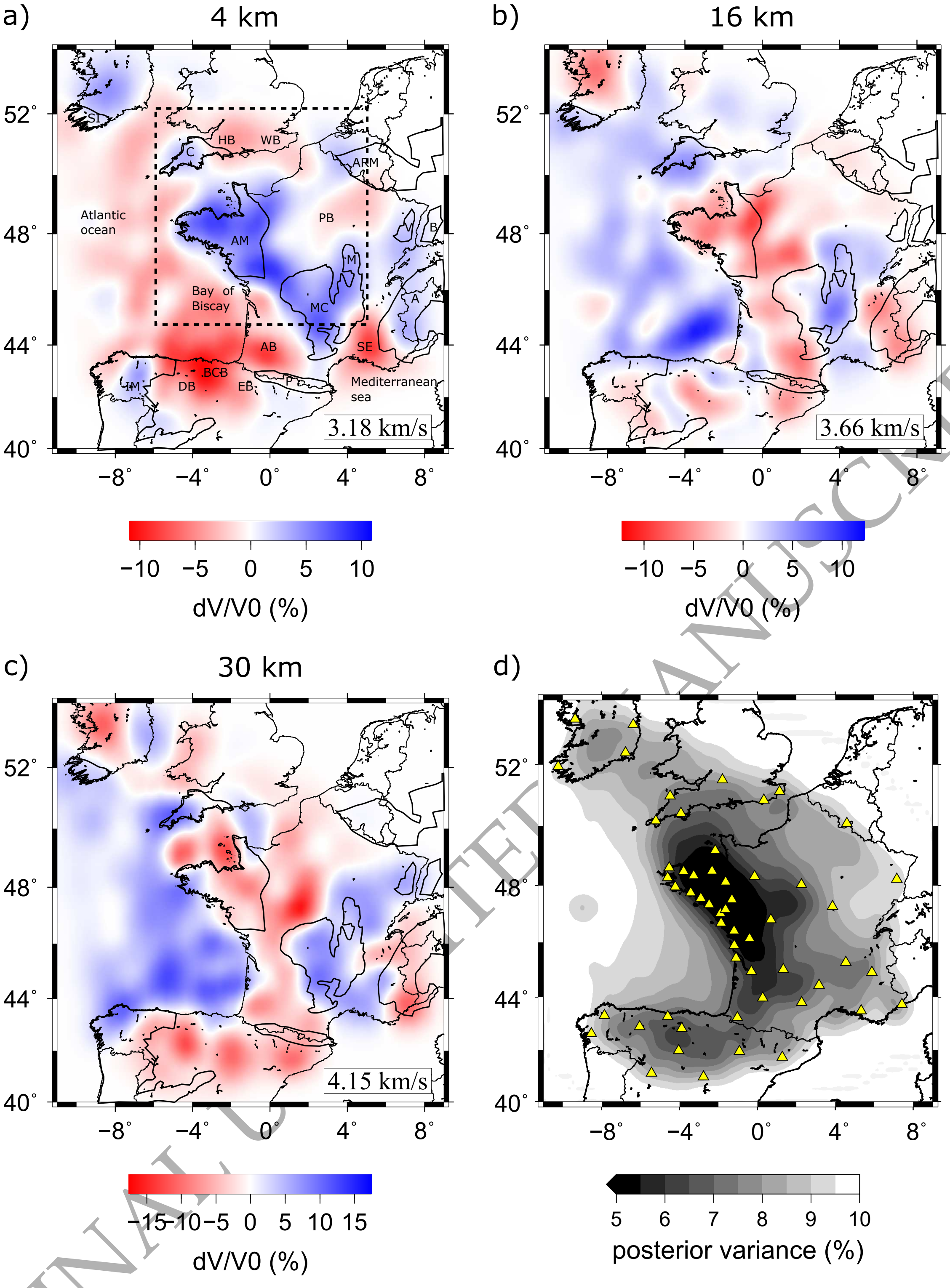

Figure 8. Isotropic V_S perturbations maps at the depths of a) 4 km, b) 16 km and c) 30 km. The median V_S value is indicated in lower right of each map. The dashed black rectangle in a) indicates the western France and the surrounding regions. The main geolocical features of the region are indicated . See Figure 1a for legend. d) *a posteriori* variance on model parameters associated with the 30 km depth result.

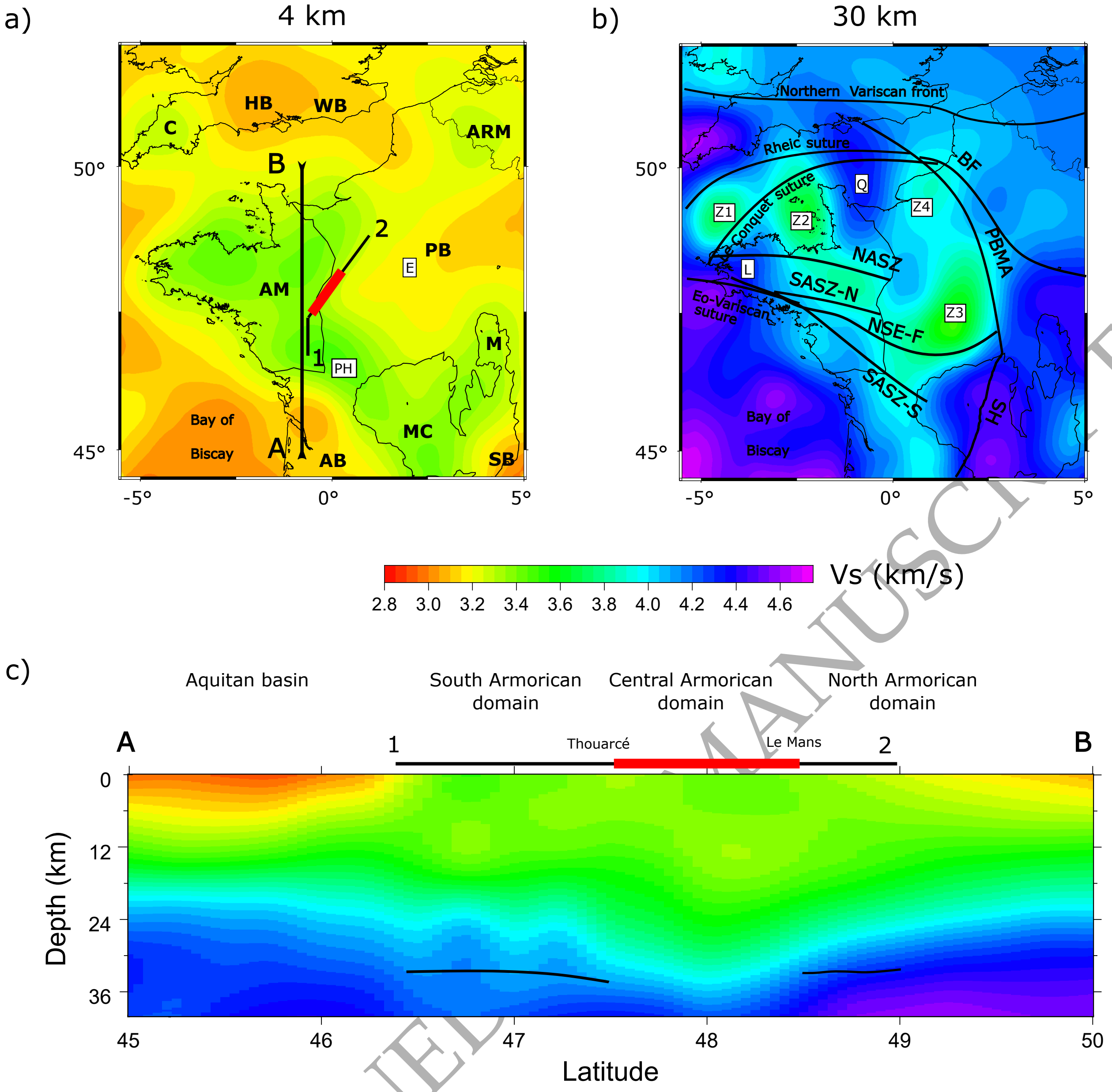

Figure 9. Isotropic V_S horizontal and vertical cross-section in the 3-D model for western France and the surrounding regions. a) 4 km horizontal cross-section. The position of the vertical cross-section presented in c) is indicated with A and B. The position of the ECORS profile [Matte & Hirn, 1988] is indicated with 1 and 2. b) 30 km horizontal cross-section. See Figure 1a for legend. Labelled white rectangles indicate specific features discussed in the text. c) Vertical cross-section at -1° longitude between 45° and 50° latitude. The continuous black lines superimposed on the section report the Moho depth detected along the ECORS profile. The red rectangle indicates the area between the cities of Thouarcé and Le Mans where anomalous reflectivity and attenuation pattern have been detected [Matte & Hirn, 1988; Campillo & Plantet, 1991]. See text for details.